1 **Analyzing the Human Liver Vascular Architecture by Combining Vascular**

2 **Corrosion Casting and Micro-CT Scanning: a Feasibility Study**

3

4 **Short running page heading**

5 "Analyzing the Human Liver Vascular Architecture"

6

7 Charlotte Debbaut[1], Patrick Segers[1], Pieter Cornillie[2], Christophe Casteleyn[3], Manuel

8 Dierick[4], Wim Laleman[5], Diethard Monbaliu[6]

9

10 [1]Biofluid, Tissue and Solid Mechanics for Medical Applications, Institute Biomedical

11 Technology, Ghent University. De Pintelaan 185 – Block B, B-9000 Gent, Belgium

12 (charlotte.debbaut@ugent.be; patrick.segers@ugent.be)

13 Telephone: 003293313137

14

15 [2]Department of Morphology, Faculty of Veterinary Medicine, Ghent University. Salisburylaan

16 133, B-9820 Merelbeke, Belgium (pieter.cornillie@ugent.be)

17 Telephone: 003292647722

18

19 [3]Laboratory of Applied Veterinary Morphology, Embryology & Pathology, Department of

20 Veterinary Sciences, Faculty of Pharmaceutical, Biomedical and Veterinary Sciences, University

21 of Antwerp. Universiteitsplein 1, 2610 Wilrijk, Belgium (christophe.casteleyn@ua.ac.be)

22   Telephone: 003232652821

23

24   [4]UGCT, Department of Physics and Astronomy, Ghent University. Proeftuinstraat 86, B-9000

25   Gent, Belgium (manuel.dierick@ugent.be)

26   Telephone: 003292646611 / 003292646532

27

28   [5] Hepatology, University Hospitals Leuven, & department Development and Regeneration, KU

29   Leuven. Herestraat 49, B-3000 Leuven, Belgium (wim.laleman@uzleuven.be)

30   Telephone: 003216344299

31

32   [6]Abdominal Transplant Surgery, University Hospitals Leuven, & department of Microbiology

33   and Immunology, KU Leuven. Herestraat 49, B-3000 Leuven, Belgium

34   (diethard.monbaliu@uzleuven.be)

35   Telephone: 003216344222

36

37   **List of abbreviations**

38   HA   Hepatic Artery / Hepatic Arterial

39   PV   Portal Vein / Portal Venous

40   HV   Hepatic Vein / Hepatic Venous

41   CT   Computer Tomography

42   DICOM   Digital Imaging and Communications in Medicine

43   VCI   Vena Cava Inferior

44   r   Radius

45 l   Length

46 n   Number of vessels

47 R^2 Coefficient of determination

48 x, f   Generation number

49

50 **There is no conflict of interest.**

51

Summary/Abstract

Introduction: Although a full understanding of the hepatic circulation is one of the keys to successfully perform liver surgery and to elucidate liver pathology, relatively little is known about the functional organisation of the liver vasculature. Therefore, we materialized and visualized the human hepatic vasculature at different scales and performed a morphological analysis by combining vascular corrosion casting with novel micro-CT and image analysis techniques.

Methods: A human liver vascular corrosion cast was obtained by simultaneous resin injection in the hepatic artery and portal vein. A high resolution (110 µm) micro-CT scan of the total cast allowed gathering detailed macrovascular data. Subsequently, a mesocirculation sample (starting at generation 5; 88 x 68 x 80 mm³) and a microcirculation sample (terminal vessels including sinusoids; 2.0 x 1.5 x 1.7 mm³) were dissected and imaged at a 71 µm and 2.6 µm resolution, respectively.

Results: Segmentations and 3D reconstructions allowed quantifying the macro- and mesoscale branching topology and geometrical features of hepatic arterial, portal venous and hepatic venous trees up to 13 generations (radii ranging from 13.2 mm to 80 µm; lengths from 74.4 mm to 0.74 mm), as well as microvascular characteristics (mean sinusoidal radius of 6.63 µm).

Conclusions: Combining corrosion casting and micro-CT imaging allows quantifying the branching topology and geometrical features of hepatic trees using a multiscale approach from the macro- down to the microcirculation. This may lead to novel insights into liver circulation, such as internal blood flow distributions and anatomical consequences of pathologies (e.g. cirrhosis).

Keywords: morphology, hepatic vasculature, image processing, 3D reconstruction, tree analysis

76 **Introduction**

77

78 The liver is a fascinating but complex multifunctional organ, characterized by its intricate

79 vascular architecture. Compared to other organs, the liver's vasculature is unique due to the two

80 blood supplies. Traditionally, the hepatic artery (HA) is regarded to supply the liver with

81 oxygenated blood. The portal vein (PV) collects partially deoxygenated blood from the intestinal

82 tract including spleen and pancreas. HA and PV blood mixes in the sinusoids, the hepatic

83 microcirculation, often portrayed as a lattice of small vessels in between rows of hepatocytes,

84 determining the smallest functional unit or liver lobule. Blood subsequently leaves liver lobules

85 through central veins and eventually drains into the vena cava inferior (VCI) via the hepatic

86 venous system (HV) (Roskams et al., 2007). All vascular trees as well as the microcirculation

87 have their own morphological and functional characteristics. Together, they determine the hepatic

88 hemodynamic behavior, such as the arterial buffer response (Eipel et al., 2010) or less

89 physiologic phenomena such as flow competition between the HA and PV (Monbaliu et al.,

90 2012).

91

92 The clinical relevance to understand the exact hepatic vascular anatomy is illustrated by the

93 disturbed vascular architecture in case of liver pathology, such as cirrhosis with fibrosis

94 (overproduction of extracellular matrix), regenerative nodules, increased vascular resistance, neo-

95 angiogenesis and vascular remodeling leading to portal hypertension and intrahepatic shunt

96 vessels (Anthony et al., 1978, Chen et al., 2009, Thabut and Shah, 2010). Moreover, the hepatic

97 vasculature is subject to intraspecies anatomical differences, relevant for transplantation. Patient-

98 specific analysis of the hepatic vascular topology through computed tomography (CT) and

99   magnetic resonance angiography may facilitate surgical planning and improve its outcome

100   (Mutter et al., 2009, Selle et al., 2002, Yamanaka et al., 2006). Furthermore, topology

101   information and geometrical characteristics may be fed to numerical models to simulate hepatic

102   hemodynamics, useful to model e.g. surgical procedures or the performance of new preservation

103   techniques for transplant livers (e.g. machine perfusion) (Debbaut et al., 2011, Bonfiglio et al.,

104   2010, Rani et al., 2006, Ricken et al., 2010, Debbaut et al., 2012b, Debbaut et al., 2012a).

105

106   Morphological analysis of vascular trees in different organs and species is not new (e.g. rodent

107   pulmonary trees (Gomes and Bates, 2002), mouse placental arteries (Rennie et al., 2011), human

108   coronary arteries (Finet et al., 2007), mouse kidneys (Wagner et al., 2011)). However, to our

109   knowledge, only a few papers were published on the liver's vasculature. Op Den Buijs et al. (Op

110   Den Buijs and Ritman, 2006) classified the PV tree of the rat liver, but not the HA or HV tree.

111   Selle et al. (Selle et al., 2002) focused on analyzing the macrocirculation for surgical planning

112   based on vascular territories. We previously performed studies on modeling liver perfusion based

113   on the macrovessel architecture of the human (Debbaut et al., 2011) and rat liver (Francque et

114   al., 2012, Debbaut et al., 2012a). A larger number of studies has been published on liver

115   microcirculation using for example microscopy, histological techniques (Teutsch et al., 1999,

116   Ekataksin and Wake, 1991, Ekataksin and Wake, 1997, Greenway and Stark, 1971, Matsumoto

117   and Kawakami, 1982, Matsumoto et al., 1979, McCuskey, 1966, McCuskey and Reilly, 1993,

118   Rappaport et al., 1954), or performing 3D reconstructions by registering 2D serial cryosections as

119   done by Teutsch et al. (Teutsch, 2005).

120

121   Until now, the total spectrum of the human liver vascular architecture has not been analyzed yet

122   in a systematic way on single liver samples. Therefore, the aim of this study was to analyze the

123   complete human liver vascular architecture using a combination of vascular corrosion casting,

124   micro-CT scanning and image processing. Hereby, a novel multiscale approach was applied to

125   consecutively analyze the macro-, meso- and microcirculation.

126

Materials and methods

127

128

129   In this study, a human liver was used after being discarded for transplantation due to failed

130   reallocation. The protocol conforms to the ethical guidelines of the 1975 Declaration of Helsinki,

131   and was approved by the Ethical Committee of the University Hospitals Leuven, Belgium, and by

132   the Belgian Liver and Intestine Committee as foreseen by the initial protocol.

133

Vascular corrosion casting

135   After hepatectomy, the liver (weight ± 1.9 kg) was connected to a machine perfusion

136   preservation device (Organ Recovery Systems, Zaventem, Belgium) during a 24h period, and was

137   continuously perfused at 4-6°C with pressure-control through the HA (25 mmHg; unlimited flow)

138   and PV (7 mmHg; flow limitation of 300 ml/min). The pressure-controlled feedback system,

139   incorporated in the perfusion machine, ensured that perfusion pressures did not exceed the

140   maximum pressure settings. Machine perfusion allowed preserving the vasculature and

141   parenchyma and keeping the blood vessels open whilst preparing the necessary logistics.

142   Subsequently, the liver was prepared for the vascular corrosion casting procedure by cannulation

143   of the HA, PV as well as the VCI. Casting resin was prepared by mixing Batson's #17 monomer

144   solution, catalyst and promoter (Polysciences, Warrington, USA) with monomeric methyl

145   methacrylate (Merck, Darmstadt, Germany) and color dyes (red and blue for the HA and PV,

146   respectively). In addition, barium sulfate (50 mg/ml; Micropaque, Delpharm, France) was added

147   to the HA injection to amplify the contrast between arterial and venous vessels on CT images,

148   facilitating to distinguish different contributing vessels. The HA and PV were simultaneously and

149   manually injected until the resin emerged sufficiently from the VCI. Afterwards, inlet and outlet

150   vessels were clamped to avoid resin leakage during polymerization of the injected mixture

151   (approximately two hours). Next, the liver was macerated in a potassium hydroxide bath

152   (approximately two days). More detailed information on the vascular corrosion procedure is

153   available in (Debbaut et al., 2011).

154

155   ***Micro-CT imaging***

156

157   *Macrocirculation*

158   The resulting human liver cast (Fig. 1a) was imaged in globo to acquire data of the first blood

159   vessel generations, being a similar number of generations as obtained with traditional

160   angiography techniques (macrocirculation; Fig. 1a). This was done using a state-of-the-art in-

161   house developed high resolution micro-CT scanner (Fig. 1d). Two thousand images were

162   recorded during a 360° rotation of the cast. The image dataset (resolution of 102 µm) was

163   reconstructed with Octopus software (Ghent University, Gent, Belgium) and converted to the

164   DICOM format. More information on the scanning procedure is available in (Debbaut et al.,

165   2011).

166

167   *Mesocirculation*

168   A smaller sample (wedge-shaped; approximately 88 mm x 68 mm x 80 mm) was dissected from

169   the inferior part of the right lobe (Fig. 1a-b) to investigate the morphology of vessel generations

170   distal to the macrocirculation. This sample was imaged at a resolution of 71 µm.

171

172   *Microcirculation*

173 Thirdly, a microvascular sample (approximately 2.0 mm x 1.5 mm x 1.7 mm) was dissected from

174 the superior part of the right lobe to study the smallest vessels of the liver (Fig. 1c). To assure that

175 the sinusoids were filled during casting, this sample was imaged by scanning electron microscopy

176 (Fig. 1c). Afterwards, the sample was imaged using the micro-CT scanner at a 2.6 μm resolution.

177

178 ***Image processing and vascular architecture analysis***

179

180 *Macrocirculation*

181 The resulting micro-CT dataset was processed using Mimics (Materialise, Leuven, Belgium). The

182 vascular trees were segmented based on the gray values of the images. Separating arterial from

183 venous vessels was straightforward due to the arterial contrast agent. It was, however,

184 challenging to segment the PV and HV trees (having similar gray values), which were manually

185 separated at locations where they touched each other. Therefore, each vascular tree was followed

186 starting at the first generation vessel going down to smaller vessels. When a touching vessel was

187 detected, it was separated by removing the pixel(s) of the connection. After segmentation, a 3D

188 reconstruction of each tree was calculated.

189 After image processing, the vascular tree centerlines were calculated using the centerline

190 algorithm in Mimics. Using the concept of blood vessel generations, the centerlines were used to

191 determine the branching topology and geometrical features of all vascular trees. This was done by

192 classifying vessels based on their branching pattern (see (Debbaut et al., 2011) for more detailed

193 information), being either *n*-furcations (parent vessels splitting in *n* similar daughter vessels

194 (dichotomous bifurcations when *n=2*) or monopodial vessels (small side branches coming of

195 parent vessels at an angle close to 90°) (Gordon et al., 2007). Hereby, the inlet vessel of each

196 vascular tree is assigned to generation 1. Daughter vessels have higher generation numbers than

197   their parent vessel. For instance, if a generation *n* vessel splits into two daughter vessels with a

198   similar smaller diameter, the daughter vessels are assigned to generation *n+1*. In addition, the

199   radius (r; best fit radius averaged over the vessel) and length (l; centerline length) of each vessel

200   were measured. After data acquisition, exponential trend lines were fitted to the data (mean

201   radius, mean length, number of vessels) as a function of the generation number (eq. 1 with *y* the

202   geometrical feature, *x* the generation number; *a* and *b* the coefficients to be fitted). Exponential

203   trend lines were selected, since they showed a better goodness of fit compared to linear and

204   power law trend lines.

$$y(x) = a\, e^{-bx} \tag{1}$$

206

207   *Mesocirculation*

208   Again, segmentations and 3D reconstructions were performed. As this sample contains vessel

209   generations distal to the macrocirculation, while the resolution is insufficient to capture the

210   microvessels, it is labeled 'mesocirculation'.

211   Vascular tree analysis of this sample was similar to that of the macrocirculation. However, for

212   labor intensity reasons, we did not analyze the total sample but selected four representative

213   subsamples (brighter subsamples in Fig. 2f-h). To register the mesocirculatory dataset with the

214   macrocirculatory dataset, the ingoing HA, PV and HV vessel of each mesocirculation subsample

215   were identified by their corresponding vessel in the macrocirculatory dataset. Doing so, it was

216   straightforward to assign generation numbers and geometrical feature measurements (radii and

217   lengths) to the mesovessels. However, since we did not quantify the total liver mesovasculature,

218   the number of vessels versus the generation number ($n_{meso,estimated}(x)$; x is the generation number)

219   had to be estimated. This was done by multiplying the measured number of vessels for each

220   mesocirculation generation ($n_{meso}(x)$) by a factor. This factor is determined by dividing the

221   number of macrocirculation vessels of the fth generation ($n_{macro}(f)$; f is the number of the first

222   mesocirculation generation included in all four subsamples) by the number of measured vessels

223   of generation f in the mesocirculation ($n_{meso}(f)$) (eq. 2).

224
$$n_{meso,estimated}(x) = n_{meso}(x) \cdot \frac{n_{macro}(f)}{n_{meso}(f)} \tag{2}$$

225

226   *Microcirculation*

227   Since, at the terminal microcirculation level (interconnected sinusoids), the difference between

228   arterial and portal vessels becomes unclear and the tree structure is lost, the dataset was

229   segmented as one volume, instead of being separated in HA, PV and HV trees. Consequently, this

230   dataset was used to investigate the hepatic vascular microstructure and its dimensions by

231   calculating 3D visualizations and measuring lobule and sinusoid diameters.

232 **Results**

233

234   The casting procedure resulted in a replica of the human hepatic vascular system (Fig. 1a). HA

235   vessels were red, while PV and HV were blue, due to the relatively high PV flow (75% of the

236   outflow) compared to HA flow, resulting in dominantly blue HV flow.

237

238   *Macrocirculation*

239   Fig. 2 shows 3D reconstructions of the total liver micro-CT scan. The HA, PV and HV vascular

240   beds were clearly distinguishable. Next to n-furcations (such as bifurcations and trifurcations),

241   the trees count a high number of monopodial vessels, sprouting from parent vessels at angles

242   close to 90° (Fig. 2b-d). After the first generations, HA vessels run parallel to PV vessels. In a

243   few cases, one PV vessel is even flanked by two HA vessels. Moreover, HA vessels have

244   predominantly circular cross-sections compared to elliptical cross-sections of PV and HV vessels.

245   This anatomical feature is probably due to the structural differences between veins (thin vessel

246   walls) and arteries (thick vessel walls including a thick muscle layer). Each tree was classified

247   according to its branching topology, resulting in 6, 6 and 5 generations for the HA, PV and HV

248   tree, respectively. Mean HA radii drop from 3.45 mm to $5.92 \cdot 10^{-1}$ mm, PV radii from 7.34 mm to

249   1.08 mm and HV radii from 13.2 mm (VCI) to 1.13 mm (Fig. 3a-c; see also Tables 1-4 in

250   (Debbaut et al., 2011)). As anticipated, portal and hepatic venous vessels (PV and HV) have

251   larger diameters compared to HA vessels. Exponential trend lines, fitted to radii measurements,

252   have high determination coefficients ($R^2 \geq 0.97$; see also Tables 1-4 in (Debbaut et al., 2011)).

253   Mean lengths don't show a clear-cut decreasing trend in the first generations (especially for PV

254   vessels), but decrease in higher generations (Fig. 3d-f). This is partially due to the first generation

255   vessel of each tree being cut to resect the liver, implying an underestimated length. Therefore, the

256   first generation length is not accounted for when calculating length trend lines. The PV length

257   trend line has the lowest R^2 value (0.77). Length standard deviations are higher than for radii.

258   Numbers of vessels per generation clearly increase exponentially towards higher generation

259   numbers: from 1 to 271, 1 to 216, and 1 to 76 vessels for the HA, PV, and HV tree, respectively

260   (Fig. 3g-i; see also Tables 1-4 in (Debbaut et al., 2011)).

261

262   *Mesocirculation*

263   Segmentations of the mesocirculation subsample (Fig. 1b) were more challenging than the

264   macrocirculation, because more vessels were touching each other (Fig. 2e-h). Fig. 1b and 2e

265   show that the PV inflow runs parallel to two HA vessels. Similar to the macrocirculation, this

266   sample shows elliptical PV and HV vessels compared to circular HA vessels. Analyzing four

267   subsamples (Fig. 2f-h) resulted in the visualization of higher generation vessels, going up to

268   generation 13, 13 and 10 for the HA, PV and HV trees, respectively (Table 1, Fig. 3). Mean radii

269   decrease to $8.00 \cdot 10^{-2}$, $1.23 \cdot 10^{-1}$and $1.60 \cdot 10^{-1}$ mm for the HA, PV and HV trees, respectively (Fig.

270   3a-c). Radii trend lines were fitted to the pooled macro- and mesocirculation measurements ($R^2 \geq$

271   0.98). Mean lengths also decrease for all trees ($R^2 \geq 0.94$). The numbers of vessels per generation

272   again increases exponentially, almost exactly following extrapolations of the macrocirculation

273   trend lines. All trend lines fitted to the combination of macro- and mesocirculation measurements

274   show equal or higher goodness of fit than those fitted to only the macrocirculation, except for the

275   HA radii (Fig. 3).

276

277   *Microcirculation*

278   Scanning electron microscopy of the microcirculation sample shows that casting resin was

279   observed in the sinusoids (Fig. 1c). The sample represents a complex network of interconnected

280   and tortuous sinusoids (Fig. 4). Measurements of one hundred sinusoids resulted in a mean

281   diameter of 13.23 ± 2.36 µm.

282

283 **Discussion**

284

285 For the first time, the total spectrum of the (human) hepatic vasculature (from the largest vessels

286 down to the sinusoidal microcirculation) is visualized and 3D reconstructed. Therefore, this pilot

287 study used a combination of state-of-the-art vascular corrosion casting and micro-CT scanning

288 techniques (at resolutions up to the order of 2.6 µm) with a novel image processing and analysis

289 technique.

290

291 However, one has to be careful when generalizing these findings based on a single liver because

292 of potential individual differences such as different vessel dimensions, different liver sizes

293 according to the body weight (the liver represents approximately 2% of the total body weight),

294 different liver shapes (e.g. a relatively small or large left lobe) and the potential presence of liver

295 pathology (e.g. fibrotic tissue and regenerative nodules in liver cirrhosis). More livers should thus

296 be similarly analyzed to get a general overview of the human hepatic vascular architecture. As

297 such, this pilot study should be interpreted as the vascular analysis of a specific liver. This human

298 liver was offered to our lab after failed rescue allocation and there was no obvious macroscopic

299 abnormality. The casting procedure was done by manual injection, having the advantage of

300 sensing how the organ reacts while injecting. Also, it has been described that casting may lead to

301 slight shrinkage of the resin, which would imply slightly smaller diameters (Kratky and Roach,

302 1984). However, our diameter measurements were comparable with literature data on the largest

303 hepatic vessels and sinusoidal diameters (Matsumoto and Kawakami, 1982, Warren et al., 2008,

304 Vollmar and Menger, 2009). Moreover, the casting procedure was performed according to

305 standardized procedures by a team having many years of expertise (Debbaut et al., 2011,

306 Casteleyn et al., 2010, Debbaut et al., 2012a).

307

308   Ideally, the complete cast should be scanned at once at a sufficiently high resolution to allow

309   visualizing all vessels down to the sinusoids. However, it was technically impossible to scan a

310   total liver at a resolution of a few micrometers due to computational and software limitations to

311   process datasets with an extremely large file size. Consequently, a multiscale approach was used

312   to consecutively study the macro-, meso- and microcirculation, allowing the quantification of 13

313   (HA and PV) and 10 (HV) blood vessel generations as well as the sinusoids. However, there is

314   still a gap of a number of generations between the $10/13^{th}$ generation and the sinusoids.

315   Nonetheless, the total number of generations can be approximated by extrapolating the resulting

316   exponential trend lines of the radius (Fig. 3) down to the level of radius values of the terminal

317   vessels, resulting in an estimation of 19-20, 17-18 and 13-14 generations for the HA, PV and HV

318   trees, respectively. Hereby, sinusoids are interpreted as being the connection between the

319   terminal/last generation of the inflow trees (HA and PV) and outflow tree (HV).

320

321   Our data reveal a complex hepatic vascular topology covering the macro- down to the

322   microcirculation, showing that hepatic trees do not solely branch according to a dichotomous

323   bifurcating pattern, which is often assumed in vascular tree models. *N*-furcations as well as

324   monopodial vessels were clearly visualized in the macro- and mesocirculation. Geometrical

325   characteristics (Fig. 3) show exponential behavior as a function of generation numbers. HA and

326   PV trees show similar behavior and exponential trends, resulting in equal numbers of generations

327   for the macro- and mesocirculation. However, PV radii are larger than HA radii, and starting

328   from generation 4, numbers of HA vessels are higher than those of PV vessels (Fig. 3 g-h, Table

329   1 and Tables 2-4 in (Debbaut et al., 2011)), probably due to some PV vessels being flanked by

330   two parallel HA vessels. The HV tree has the largest radii and typically counts less generations

331 than the HA and PV tree.

332

333 In contrast, the microcirculation gives evidence of a completely different type of organization

334 compared to vascular trees. Tortuous sinusoids form an interconnected and intertwined network

335 embedded in a matrix of liver cells. Consequently, the exponential behavior of the HA, PV and

336 HV trees probably stops at the level of the terminal microcirculation (where blood is drained

337 from the terminal hepatic arterioles and portal venules into the sinusoids). From our data, macro-

338 and mesovessels may be interpreted as "distributing" vessels, ensuring that blood reaches all liver

339 lobules, and the sinusoids may be interpreted as "functional" vessels, ensuring that blood solutes

340 are able to penetrate through sinusoidal fenestrations into the space of Disse and reach the

341 microvilli of hepatocytes for metabolic exchange. The microvascular sample clearly shows

342 sinusoidal structures (Fig. 1c; meaning that the casting resin was able to fill the sinusoids) and is

343 thought to include three liver lobules. Hereby, the vascular septa of lobules seem to be

344 highlighted by contrast agent particles (bright dots in Fig. 4a). These particles are probably not

345 able to penetrate into the sinusoids because of their size, leaving them trapped at the vascular

346 septa, (partially) delineating the lobule borders (Fig. 4b). Accordingly, the sample represents

347 three liver lobules (Fig. 4a-b) and based on these contours, lobule diameters were in the order of

348 700-800 µm. As illustrated, it is not obvious to distinguish between neighboring lobules. This

349 might be due to the fact that the human liver microcirculation is characterized by less connective

350 tissue delineating its lobule borders in comparison with pig or rodent livers, often used as animal

351 liver models. Furthermore, lobules can have more irregular shapes than the traditionally

352 hexagonal prism-shaped lobules. Concerning this, literature gives evidence of an ongoing

353 discussion on the most appropriate functional unit to represent the liver microcirculation (e.g.

354 hexagonal lobule, primary lobule, liver acinus) (Roskams et al., 2007).

355

356   The novel and detailed morphological data gathered in this study are useful to complement

357   scientific insights into liver morphology and physiology. The new multiscale approach is also

358   applicable in the context of liver pathophysiology, e.g. to investigate pathology-related

359   microvascular alterations in case of fibrosis and cirrhosis (Chen et al., 2009, Vanheule et al.,

360   2008), hepatocellular carcinoma (Maksan et al., 2003), portal hypertension (Fondevila et al.,

361   2010, Yagi et al., 2005). Furthermore, this approach may generate input data for the development

362   of numerical models of liver perfusion. These models can be applied to simulate the

363   hemodynamic impact of (ab)normal situations such as isolated organ perfusion and surgical

364   procedures, e.g. partial hepatectomy. Microcirculation morphological data enable gaining more

365   insight into structural-related characteristics (porosity, permeability tensor) which allow

366   capturing and modeling the microcirculation behavior (especially relevant when studying

367   microvascular alterations caused by e.g. cirrhosis).

368

369 **Concluding remarks**

370

371 In conclusion, combining vascular corrosion casting with state-of-the-art high resolution micro-

372 CT scanning provides novel and unique data on the human hepatic vasculature from the

373 macrocirculation down to the microcirculation. A new multiscale approach allows visualizing the

374 complex liver vasculature at different levels in 3D and performing a detailed analysis of the

375 topology and geometrical features. These data are useful to create numerical models of the

376 hepatic blood circulation. This approach could also be applied to other organs, such as kidneys.

377

378 **Acknowledgements**

379

383   **References**

384

385   Anthony PP, Ishak KG, Nayak NC, Poulsen HE, Scheuer PJ, Sobin LH (1978) Morphology of

386   cirrhosis. *Journal of Clinical Pathology,* **31,** 395-414.

387   Bonfiglio A, Leungchavaphongse K, Repetto R, Siggers JH (2010) Mathematical modeling of the

388   circulation in the liver lobule. *Journal of Biomechanical Engineering,* **132,** 111011.

389   Casteleyn C, Trachet B, Van Loo D, et al. (2010) Validation of the murine aortic arch as a model

390   to study human vascular diseases. *Journal of Anatomy,* **216,** 563-571.

391   Chen ML, Zeng QY, Huo JW, Yin XM, Li BP, Liu JX (2009) Assessment of the hepatic

392   microvascular changes in liver cirrhosis by perfusion computed tomography. *World*

393   *Journal of Gastroenterology,* **15,** 3532-3537.

394   Debbaut C, De Wilde D, Casteleyn C, et al. (2012a) Modeling the Impact of Partial Hepatectomy

395   on the Hepatic Hemodynamics Using a Rat Model. *Ieee Transactions on Biomedical*

396   *Engineering,* **59,** 3293-3303.

397   Debbaut C, Monbaliu D, Casteleyn C, et al. (2011) From vascular corrosion cast to electrical

398   analog model for the study of human liver hemodynamics and perfusion. *IEEE*

399   *Transactions on Biomedical Engineering,* **58,** 25-35.

400   Debbaut C, Vierendeels J, Casteleyn C, et al. (2012b) Perfusion characteristics of the human

401   hepatic microcirculation based on three-dimensional reconstructions and computational

402   fluid dynamic analysis. *Journal of Biomechanical Engineering,* **134**.

403   Eipel C, Abshagen K, Vollmar B (2010) Regulation of hepatic blood flow: The hepatic arterial

404   buffer response revisited. *World Journal of Gastroenterology,* **16,** 6046-6057.

405   Ekataksin W, Wake K (1991) Liver units in 3 dimensions: 1. Organization of argyrophilic

406   connective-tissue skeleton in porcine liver with particular reference to the compound

407   hepatic lobule. *American Journal of Anatomy,* **191,** 113-153.

408   Ekataksin W, Wake K (1997) New concepts in biliary and vascular anatomy of the liver.

409   *Progress in Liver Diseases* **15,** 1-30.

410   Finet G, Gilard M, Perrenot B, et al. (2007) Fractal geometry of arterial coronary bifurcations: a

411   quantitative coronary angiography and intravascular ultrasound analysis. *EuroInvention,*

412   **3,** 490-498.

413   Fondevila C, Hessheimer AJ, Taura P, et al. (2010) Portal hyperperfusion: mechanism of injury

414   and stimulus for regeneration in porcine small-for-size transplantation. *Liver*

415   *Transplantation,* **16,** 364-374.

416   Francque S, Laleman W, Verbeke L, et al. (2012) Increased intrahepatic resistance in severe

417   steatosis: endothelial dysfunction, vasoconstrictor overproduction and altered

418   microvascular architecture. *Laboratory Investigation,* **92,** 1428-1439.

419   Gomes RFM, Bates JHT (2002) Geometric determinants of airway resistance in two isomorphic

420   rodent species. *Respiratory Physiology & Neurobiology,* **130,** 317-325.

421   Gordon Z, Elad D, Almog R, Hazan Y, Jaffa AJ, Eytan O (2007) Anthropometry of fetal

422   vasculature in the chorionic plate. *Journal of Anatomy,* **211,** 698-706.

423   Greenway CV, Stark RD (1971) Hepatic vascular bed. *Physiological Reviews,* **51,** 23-65.

424   Kratky RG, Roach MR (1984) Shrinkage of Batsons and its relevance to vascular casting.

425   *Atherosclerosis,* **51,** 339-341.

426   Maksan SM, Paulo H, Ryschich E, et al. (2003) In vivo assessment of angioarchitecture and

427   microcirculation in experimental liver cancer - a new model in rats. *Digestive Diseases*

428   *and Sciences,* **48,** 279-290.

429   Matsumoto T, Kawakami M (1982) The unit-concept of hepatic parenchyma - a re-examination

430   based on angioarchitectural studies. *Acta Pathologica Japonica,* **32,** 285-314.

431   Matsumoto T, Komori R, Magara T, et al. (1979) A study on the normal structure of the human

432   liver, with special reference to its angioarchitecture. *Jikeikai Medical* **26,** 1-40.

433   McCuskey RS (1966) A dynamic and static study of hepatic arterioles and hepatic sphincters.

434   *American Journal of Anatomy,* **119,** 455-477.

435   McCuskey RS, Reilly FD (1993) Hepatic microvasculature: dynamic structure and its regulation.

436   *Seminars in Liver Disease,* **13,** 1-12.

437   Monbaliu D, Debbaut C, Hillewaert W, et al. (2012) Flow competition between hepatic arterial

438   and portal venous flow during hypothermic machine perfusion preservation of porcine

439   livers. *International Journal of Artificial Organs,* **35,** 119-131.

440   Mutter D, Dallemagne B, Bailey C, Soler L, Marescaux J (2009) 3D virtual reality and selective

441   vascular control for laparoscopic left hepatic lobectomy. *Surgical Endoscopy and Other*

442   *Interventional Techniques,* **23,** 432-435.

443   Op Den Buijs JB, Z., Ritman EL (2006) Branching morphology of the rat hepatic portal vein tree:

444   a micro-CT study. *Annals of Biomedical Engineering,* **34,** 1420-1428.

445   Rani HP, Sheu TWH, Chang TM, Liang PC (2006) Numerical investigation of non-Newtonian

446   microcirculatory blood flow in hepatic lobule. *Journal of Biomechanics,* **39,** 551-563.

447   Rappaport AM, Borowy ZJ, Lougheed WM, Lotto WN (1954) Subdivision of hexagonal liver

448   lobules into a structural and functional unit; role in hepatic physiology and pathology.

449   *Anatomical record,* **119,** 11-33.

450   Rennie MY, Detmar J, Whiteley KJ, et al. (2011) Vessel tortuosity and reduced vascularization

451   in the fetoplacental arterial tree after maternal exposure to polycyclic aromatic

452   hydrocarbons. *American Journal of Physiology-Heart and Circulatory Physiology,* **300,**

453   H675-H684.

454   Ricken T, Dahmen U, Dirsch O (2010) A biphasic model for sinusoidal liver perfusion

455   remodeling after outflow obstruction. *Biomechanics and Modeling in Mechanobiology,* **9,**

456   435-450.

457   Roskams T, Desmet VJ, Verslype C (2007) Development, structure and function of the liver. In

458   *MacSween's Pathology of the liver* (eds Burt AD, Portmann BC, Ferrell LD), pp. 1-72.

459   Churchill Livingstone.

460   Selle D, Preim B, Schenk A, Peitgen H-O (2002) Analysis of vasculature for liver surgical

461   planning. *Ieee Transactions on Medical Imaging,* **21,** 1344-1357.

462   Teutsch HF (2005) The modular microarchitecture of human liver. *Hepatology,* **42,** 317-325.

463   Teutsch HF, Schuerfeld D, Groezinger E (1999) Three-dimensional reconstruction of

464   parenchymal units in the liver of the rat. *Hepatology,* **29,** 494-505.

465   Thabut D, Shah V (2010) Intrahepatic angiogenesis and sinusoidal remodeling in chronic liver

466   disease: New targets for the treatment of portal hypertension? *Journal of Hepatology,* **53,**

467   976-980.

468   Vanheule E, Geerts AM, Van Huysse J, et al. (2008) An intravital microscopic study of the

469   hepatic microcirculation in cirrhotic mice models: relationship between fibrosis and

470   angiogenesis. *International Journal of Experimental Pathology,* **89,** 419-432.

471   Vollmar B, Menger MD (2009) The hepatic microcirculation: mechanistic contributions and

472   therapeutic targets in liver injury and repair. *Physiological Reviews,* **89,** 1269-1339.

473   Wagner R, Van Loo D, Hossler F, Czymmek K, Pauwels E, Van Hoorebeke L (2011) High-

474   resolution imaging of kidney vascular corrosion casts with nano-CT. *Microscopy and*

475   *Microanalysis,* **17,** 215-219.

476   Warren A, Chaberek S, Ostrowski K, et al. (2008) Effects of old age on vascular complexity and

477   dispersion of the hepatic sinusoidal network. *Microcirculation,* **15,** 191-202.

478   Yagi S, Lida T, Taniguchi K, et al. (2005) Impact of portal venous pressure on regeneration and

479   graft damage after living-donor liver transplantation. *Liver Transplantation,* **11,** 68-75.

480   Yamanaka J, Saito S, Iimuro Y, et al. (2006) The impact of 3-D virtual hepatectomy simulation

481   in living-donor liver transplantation. *Journal of Hepato-Biliary-Pancreatic Surgery,* **13,**

482   363-369.

483

484

Tables

Table 1. Overview of the mesoscale HA, PV and HV measurements. Mean radii, mean lengths and numbers of vessels are reported per generation number. (Estimated numbers of vessels of mesocirculation generations are calculated using eq. 2.)

	Generation number	Mean radius [mm]	Standard deviation of radius [mm]	Mean length [mm]	Standard deviation of length [mm]	Number of vessels	Estimated number of vessels
HA Mesoscale	HA 5	$8.62\cdot10^{-1}$	$3.54\cdot10^{-3}$	54.4	25.4	2	
	HA 6	$5.21\cdot10^{-1}$	$1.54\cdot10^{-1}$	12.2	8.29	6	
	HA 7	$3.45\cdot10^{-1}$	$3.90\cdot10^{-2}$	7.22	4.04	12	542
	HA 8	$2.77\cdot10^{-1}$	$4.70\cdot10^{-2}$	3.51	2.62	34	1536
	HA 9	$2.41\cdot10^{-1}$	$4.19\cdot10^{-2}$	3.09	2.08	76	3433
	HA 10	$2.08\cdot10^{-1}$	$2.73\cdot10^{-2}$	2.36	1.38	198	8943
	HA 11	$1.60\cdot10^{-1}$	$2.62\cdot10^{-2}$	1.48	1.05	342	15447
	HA 12	$1.19\cdot10^{-1}$	$2.47\cdot10^{-2}$	1.00	$5.45\cdot10^{-1}$	225	10163
	HA 13	$8.00\cdot10^{-2}$	$2.46\cdot10^{-2}$	$7.41\cdot10^{-1}$	$2.40\cdot10^{-1}$	9	407
PV Mesoscale	PV 5	1.41	0	19.9	0	1	
	PV 6	$8.86\cdot10^{-1}$	$2.25\cdot10^{-1}$	14.8	7.94	5	
	PV 7	$7.18\cdot10^{-1}$	$1.72\cdot10^{-1}$	8.14	4.33	10	432
	PV 8	$4.82\cdot10^{-1}$	$1.12\cdot10^{-1}$	5.24	2.80	31	1339
	PV 9	$3.09\cdot10^{-1}$	$6.16\cdot10^{-2}$	3.16	1.80	86	3715
	PV 10	$2.31\cdot10^{-1}$	$3.92\cdot10^{-2}$	2.68	1.39	244	10541
	PV 11	$1.75\cdot10^{-1}$	$2.61\cdot10^{-2}$	1.48	$8.75\cdot10^{-1}$	555	23976
	PV 12	$1.38\cdot10^{-1}$	$2.39\cdot10^{-2}$	1.03	$4.91\cdot10^{-1}$	73	3154
	PV 13	$1.23\cdot10^{-1}$	$2.71\cdot10^{-2}$	$9.50\cdot10^{-1}$	$3.79\cdot10^{-1}$	6	259
HV Mesoscale	HV 5	1.27	$4.42\cdot10^{-1}$	32.5	12.7	4	
	HV 6	$7.41\cdot10^{-1}$	$9.27\cdot10^{-2}$	8.56	5.30	9	171
	HV 7	$4.56\cdot10^{-1}$	$9.66\cdot10^{-2}$	6.59	3.23	26	494
	HV 8	$2.46\cdot10^{-1}$	$7.65\cdot10^{-2}$	4.09	1.97	111	2109
	HV 9	$1.71\cdot10^{-1}$	$5.59\cdot10^{-2}$	2.61	1.47	74	1406
	HV 10	$1.60\cdot10^{-1}$	$6.10\cdot10^{-2}$	2.17	1.06	20	380

490   **Figure legends**

491

492   **Figure 1. Human liver vascular corrosion cast and micro-CT scanner.** (A) Total liver with

493   indication of the dissection location of the mesocirculation sample; (B) mesocirculation sample;

494   (C) scanning electron microscopic image of the microcirculation sample; (D) micro-CT scanner

495   with a static X-ray tube, a static flat panel detector and a rotating liver cast to capture images

496   during a 360° rotation.

497   **Figure 2. 3D reconstructions of the macrocirculation and mesocirculation.** (A) Superposition

498   of three macrovascular trees with indication of the dissection location of the mesocirculation

499   sample; macrovascular HA (B), PV (C) and HV trees (D) with arrows indicating monopodial

500   branches; (E) superposition of three mesovascular trees; mesovascular HA (F), PV (G) and HV

501   trees (H) with brighter parts indicating four subsamples used to acquire geometrical data.

502   **Figure 3. Results of the vascular tree analysis of the macro- and mesocirculation.** Radius (A-

503   C), length (D-F) and number of vessels (G-I) as a function of the generation number for the HA,

504   PV and HV trees. Macro-circulation measurements (as obtained in (Debbaut et al., 2011)) and

505   mesocirculation measurements are indicated by black and white markers, respectively. (Original

506   and estimated numbers of vessels for the mesocirculation (Table 1) are indicated by gray and

507   white dots, respectively). Exponential trend lines are depicted by dashed lines when fitted to

508   macro- and mesocirculation data. Equations and coefficients of determination (R^2) of the

509   exponential functions are given. The first HV generation (VCI) was not taken into accounted

510   when fitting the radius trend line, since the VCI has a much larger diameter and is not really part

511   of the hepatic vasculature. Length trend lines did not incorporate the first generation, since these

512   vessels were cut to resect the liver, resulting in an underestimated length.

513   **Figure 4. Liver microcirculation.** (A) Single micro-CT slice showing bright spots (probably

514   contrast agent particles); (B) indication of the most likely lobule borders; (C) 3D reconstruction

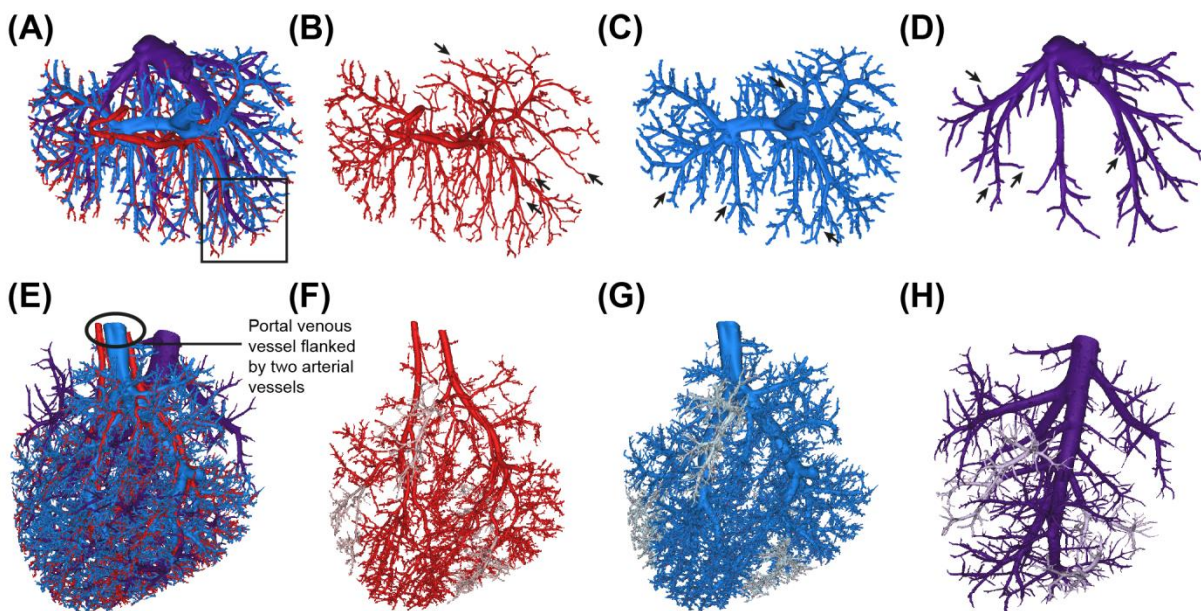515   of the microcirculation sample and (D) of a virtually dissected cubic subsample.

516

517 **Figures**

518 **Figure 1.**
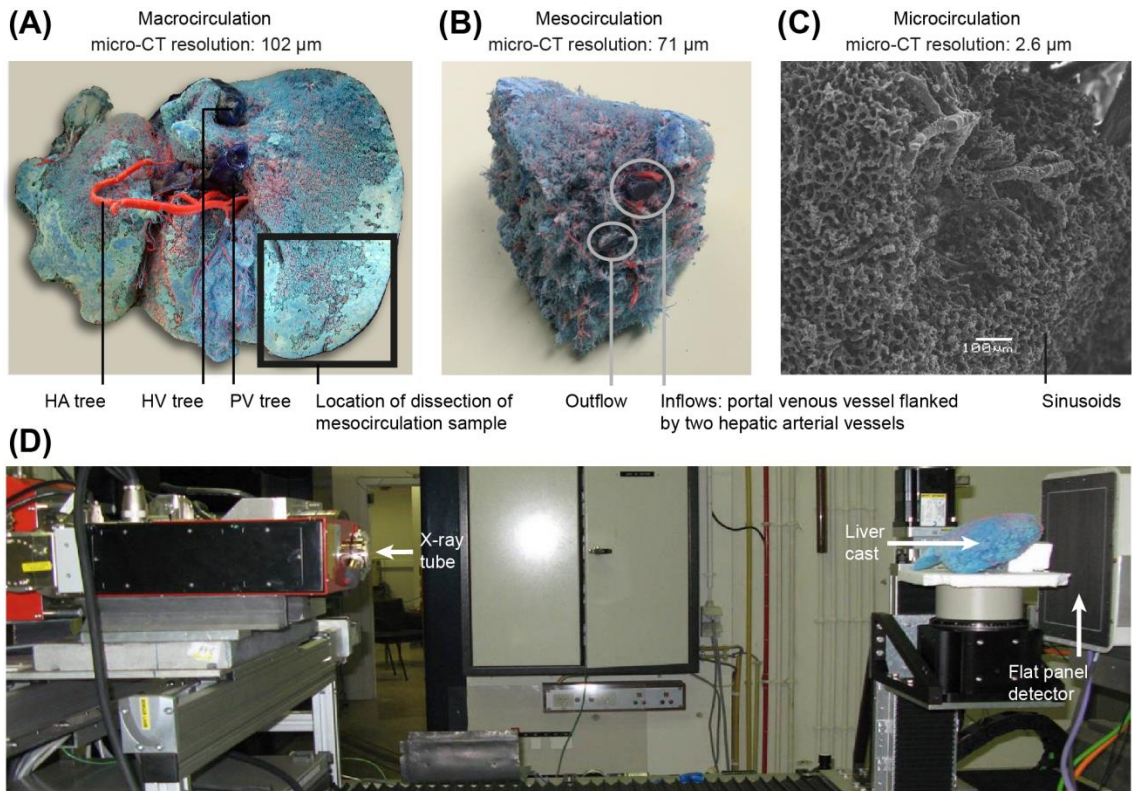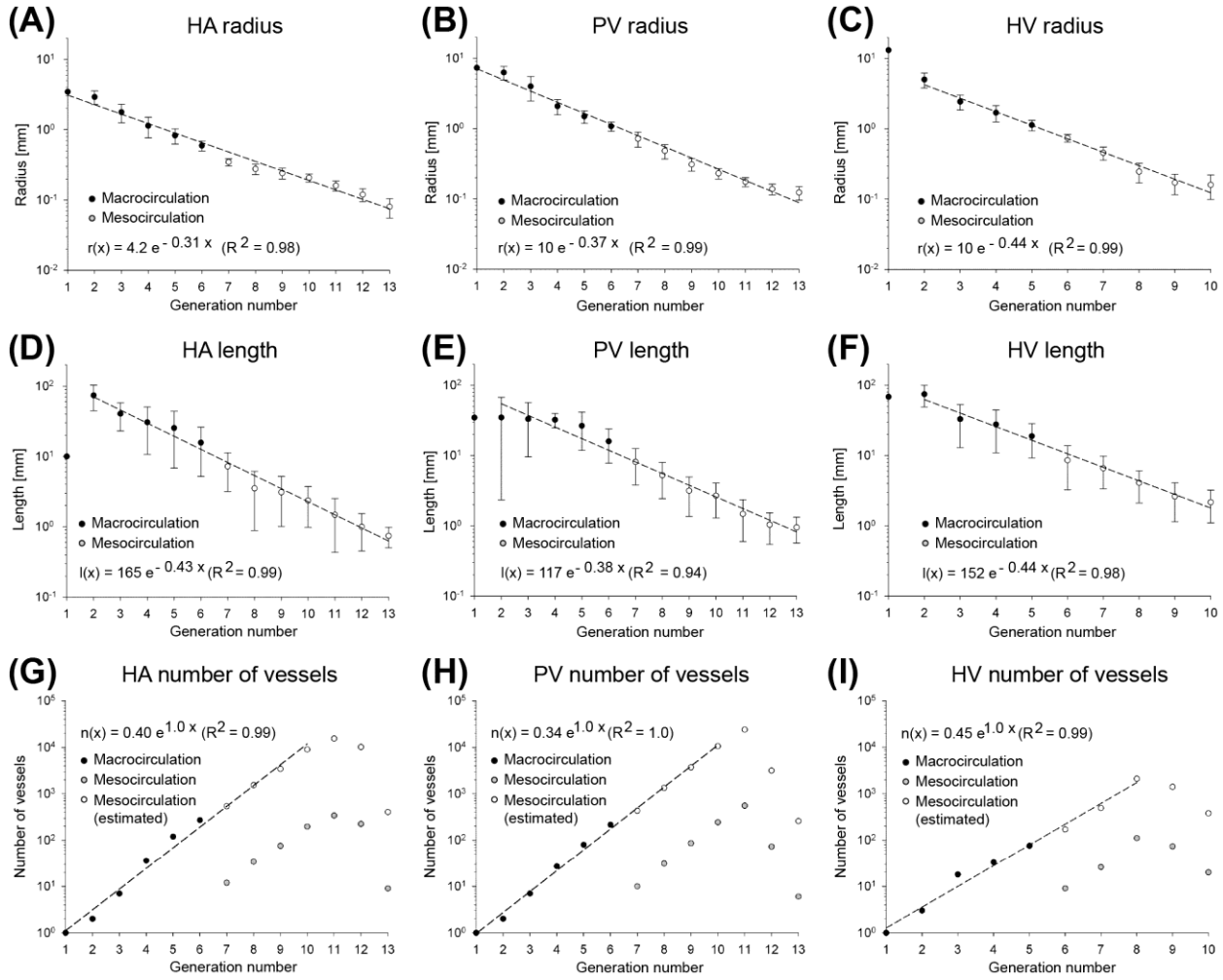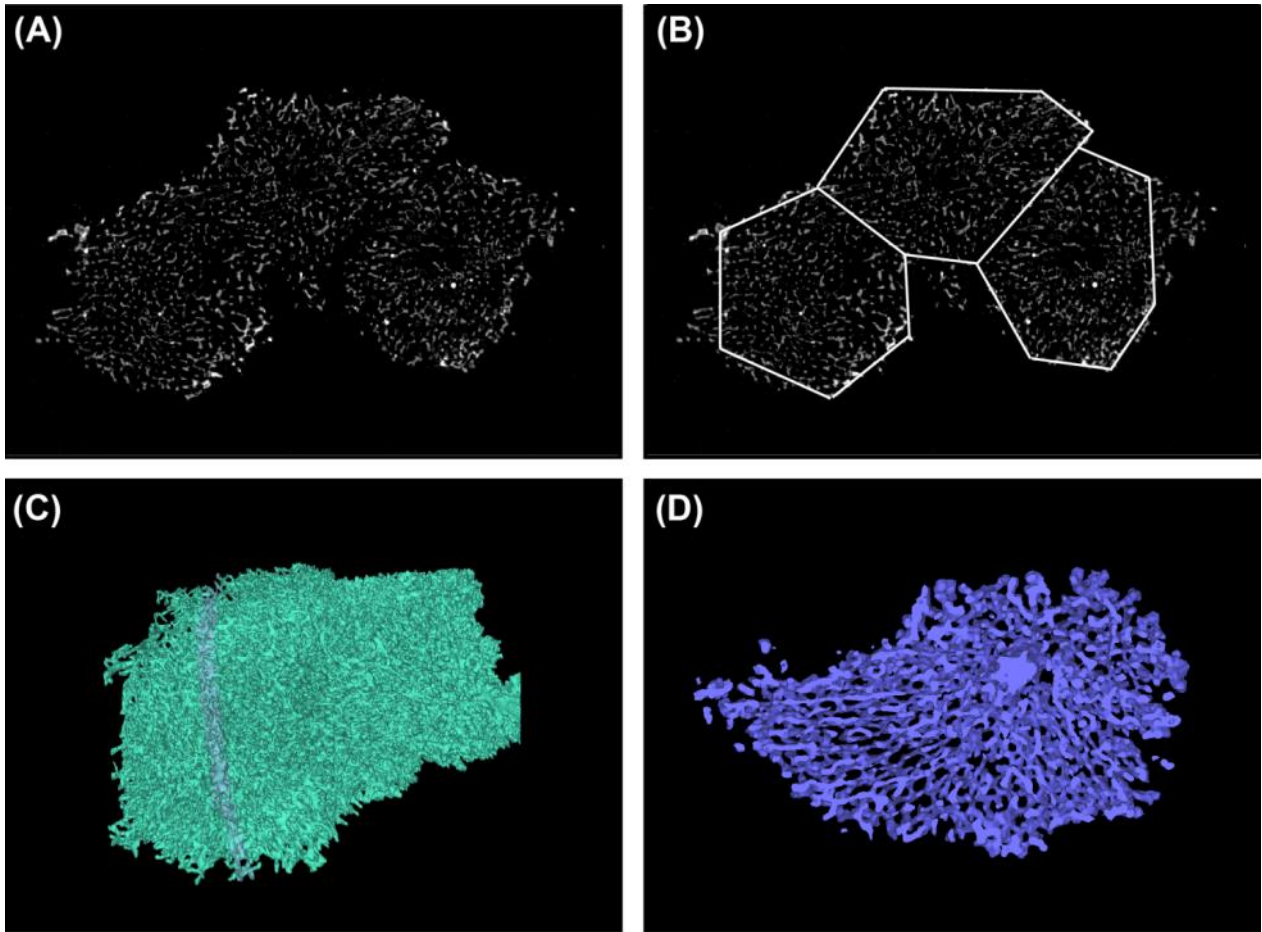

519

520

521 **Figure 2.**

522

523   **Figure 3.**

524

525

526

527 **Figure 4.**

528

529